

Efficient Nonthermal Ion and Electron Acceleration Enabled by the Flux-Rope Kink Instability in 3D Nonrelativistic Magnetic Reconnection

Qile Zhang, Fan Guo, William Daughton, and Hui Li
 Los Alamos National Laboratory, Los Alamos, NM 87545, USA*

Xiaocan Li
 Dartmouth College, Hanover, NH 03755, USA
 (Dated: November 1, 2021)

The relaxation of field-line tension during magnetic reconnection gives rise to a universal Fermi acceleration process involving the curvature drift of particles. However, the efficiency of this mechanism is limited by the trapping of energetic particles within flux ropes. Using 3D fully kinetic simulations, we demonstrate that the flux-rope kink instability leads to field-line chaos in weak-guide-field regimes where the Fermi mechanism is most efficient, thus allowing particles to transport out of flux ropes and undergo further acceleration. As a consequence, both ions and electrons develop clear power-law energy spectra which contain a significant fraction of the released energy. The low-energy bounds are determined by the injection physics, while the high-energy cutoffs are limited only by the system size. These results have strong relevance to observations of nonthermal particle acceleration in both the magnetotail and solar corona.

Introduction.— Within space and astrophysical plasmas, the magnetic field often develops stressed current sheets which are susceptible to magnetic reconnection – a process that rapidly reconfigures the magnetic topology leading to high-speed flows, plasma heating, and nonthermal particle acceleration [1]. Understanding this particle acceleration physics has immediate applications to the Earth’s magnetosphere and solar flares, and a wide variety of astrophysical problems throughout the universe. Observations from both the solar corona [2–5] and the magnetotail [6, 7] show the simultaneous production of ion and electron power-law energy distributions extending to high energy during magnetic reconnection, suggesting a common physical origin. However, the underlying physics remains poorly understood, since researchers have previously failed to produce these power-laws within self-consistent kinetic simulations in the relevant regime.

On the theoretical front, previous studies have demonstrated a Fermi-type mechanism within reconnection layers [8–13], involving the particle curvature drift within the electric field induced by the large-scale flows. This mechanism driven by field-line curvature is efficient for low guide field (out of the reconnection plane) to reconnection field ratio $b_g < 0.5$ [11–14], and is enhanced by the magnetic island interaction within the reconnection layer. However, in 2D simulations, the efficiency of the Fermi acceleration is limited by the trapping of energetic particles within these islands. Several 3D studies have demonstrated that overlapping tearing islands due to multiple resonance surfaces lead to field-line chaos [15–18], allowing energetic particles to transport out of the flux ropes and continue acceleration [10, 13, 19]. However, this mechanism only applies to regimes with significant guide fields ($b_g > 0.5$) where the efficiency of the Fermi mechanism is dramatically reduced.

In this Letter, we demonstrate with 3D kinetic simu-

lations that within the weak-guide-field regime the flux ropes are unstable to the flux-rope kink instability. This generates strong field-line chaos, allowing energetic particles to transport out of flux ropes and continue their Fermi acceleration. The field-line chaos is triggered when the flux ropes reach a threshold length for the $m = 1$ kink instability. Our 3D simulations exploiting this threshold reach an unprecedented reconnection domain. For the first time, both protons and electrons develop clear and sustainable nonthermal power-law distributions. The resulting nonthermal populations contain a significant fraction of the released energy, and remarkably, nonthermal protons gain much more energy than nonthermal electrons. The acceleration processes include an injection followed by a prolonged Fermi acceleration phase. While the injection sets the low-energy bounds of the power-laws which controls the nonthermal energy contents, the high-energy cutoffs keep growing with system size, indicating that the results can be extended to macroscopic systems.

Numerical Simulations.— We use VPIC code that solves the Vlasov-Maxwell equations [20]. The 3D simulations start from a force-free layer $\mathbf{B} = B_0 \tanh(z/\lambda) \mathbf{e}_x + \sqrt{B_0^2 \text{sech}^2(z/\lambda) + B_g^2} \mathbf{e}_y$ with a uniform plasma density $n_i = n_e = n_0$, where B_0 is the reconnecting field, B_g is the guide field and λ is the half thickness of the current sheet. λ is set to be one ion inertial length d_i . Electrons carry the initial current that satisfies the Ampere’s law. Most simulations presented here have proton-to-electron mass ratio $m_i/m_e = 25$, $b_g = B_g/B_0 = 0.2$ and $V_A = B_0/\sqrt{4\pi n_0 m_i} = 0.2c$, where c is speed of the light. The initial temperature $T_i = T_e = 0.01 m_i V_A^2$ so the plasma β based on the reconnecting magnetic field $\beta = 0.02$. The ratio of electron plasma frequency and electron gyrofrequency $\omega_{pe}/\Omega_{ce} = 1$. The grid size is taken to be $\Delta x = \Delta y = \Delta z = 0.0488 d_i$, with

150 particles per cell per species. Boundary conditions are periodic in x and y , and conducting for fields and reflecting for particles in the z -direction. A small long-wavelength perturbation is included to initiate reconnection. To limit the influence of periodic boundaries, all simulations terminate around 1.3 Alfvén crossing time L_x/V_A before the acceleration stagnates. A large set of simulations have been conducted to confirm the robustness of the underlying processes for different guide field, plasma β , domain sizes, and mass ratios, which are summarized in the Supplemental Material.

Kink Instability and Threshold for 3D Effects.— Figure 1(a) shows volume rendering of the magnitude of current density of flux ropes at $\Omega_{ci}t = 100$ in a simulation with $L_x \times L_y \times L_z = 150 \times 12.5 \times 62.5d_i^3$ [21]. The flux ropes undergo $m = 1$ kink instability and its nonlinear evolution tears up the flux surfaces (see also the supplemental movie). For comparison, flux ropes in the simulation with $L_y = 6.25d_i$ (same L_x and L_z) do not have such dynamics (Figure 1(b) [22]), although high harmonic kink modes may develop. Figure 1(c) and (d) show the y -averaged energetic electron density ($1.2 < \varepsilon/m_i V_A^2 < 2.4$) of these two simulations, overplotted with Poincaré-type plots from magnetic field lines. Figure 1(c) shows that the kink instability drives strong field-line chaos mixing up different flux surfaces while Figure 1(d), in contrast, is nearly laminar.

The transition into the field-line chaos takes place when L_y reached a threshold L_{th} , controlled by the criterion of $m = 1$ kink disruption, namely the safety factor at the edge of flux ropes $q_c = \pi b_g D / L_{th} \sim 1$ [23], where D is the diameter of the flux rope. Closer examination finds $D \sim 15d_i$ and $L_{th} \sim 9.5d_i$, placing the $L_y = 12.5d_i$ case above the threshold and the other one below it, consistent with the observed dynamics. In Supplemental Material, we systematically verified this threshold and field-line chaos driven by the kink instability in the low-guide-field regime ($b_g < 0.5$) [24].

The field-line chaos leads to particle transport out of flux ropes and further acceleration in the reconnection layer. Figure 1(c) also shows energetic electrons spreading out of flux ropes, whereas in Figure 1(d) the electrons are effectively trapped in the flux ropes. The chaotic fields can be further understood by field-line separations, namely the distances between field-line pairs with small initial displacements [25, 26]. Figure 2(a) shows the averaged separation of 10^3 field-line pairs, starting from the center of flux ropes with $D \sim 15d_i$ (e.g., $x \sim 58d_i$ in Figure 1(c) and $x \sim 73d_i$ in Figure 1(d)) for several simulations with different L_y (the same L_x and L_z as Figure 1). Above-threshold cases are far more chaotic (faster separation) than those below the threshold. To better quantify particle transport, we also trace test-particle electrons with an isotropic initial velocity $V \sim 3.5V_A$ from centers of the flux ropes (Figure 2(b)). Above-threshold cases consistently show stronger transport leaving

the center of flux ropes. To understand the transport mechanism, we calculate the displacement assuming particles just stream along field lines with a parallel speed $V_{\parallel} = 2V_A$ (root-mean-square value of the test-particle parallel velocities), which shows a trend similar to the test-particles (Figure 2(b)). This suggests that parallel streaming along the chaotic field lines is an important mechanism for particles to transport out of the flux ropes. Particle transport enabled by flux-rope kink instability greatly enhance the efficiency of particle acceleration (Figure 2(c)). Above-threshold cases consistently produce up to ~ 10 times more energetic particles (at energies ~ 100 times of the initial thermal energy) than the 2D case, whereas below-threshold cases only show moderate increase.

Simultaneous Nonthermal Acceleration of Protons and Electrons.— For larger reconnection domains, $L_{th} \sim \pi b_g D \sim 0.1\pi b_g L_x$ as D grows with L_x , which is verified by simulations with different system sizes. Our 3D simulations exploiting this condition extend to an unprecedented reconnection domain ($L_x \times L_y \times L_z = 300 \times 25 \times 125d_i^3$). We discuss nonthermal particle acceleration revealed by this simulation.

Figure 3 (a) and (b) show the time evolution of energy spectra for electrons and protons with their spectral indices shown in the corresponding insets, respectively. Both electrons and protons evolve into clear power-law distributions. While a smaller simulation ($L_x = 150d_i$) shows variable indices, the largest simulation shows that both electrons and protons sustain steady spectral indices until the end of the simulation. Interestingly, the proton spectrum is slightly harder than that of electrons, but took longer to settle into a steady power-law ($\Omega_{ci}t \sim 225$), which has been challenging to achieve in previous 3D simulations. The low-energy bounds of the power-laws are nearly constants $\varepsilon_{le} \sim 0.2m_i V_A^2$ (electron) and $\varepsilon_{li} \sim 0.5m_i V_A^2$ (proton) over time. Meanwhile, the high-energy cutoffs persistently increase with longer simulation time and larger domains (Figure 3(c)), reaching ~ 500 times of the initial thermal energy. This suggests that the nonthermal spectra can extend to much higher energies in macroscopic systems.

The first-ever proton and electron power-law distributions in kinetic simulations reveal the properties of the nonthermal components in magnetic reconnection. We determine the reconnected population by subtracting the cold upstream thermal distribution from the distribution integrated over the whole domain. Out of this population, $\sim 20\%$ of particles and $\sim 50\%$ of energy for each species are nonthermals above the low-energy bounds. This efficiency is consistent with what observed during solar flare reconnection [14, 27–29]. Energetic protons gain about twice as much energy as electrons, likely due to a more efficient injection process, as we will discuss later.

In contrast, the spectra for below-threshold cases do

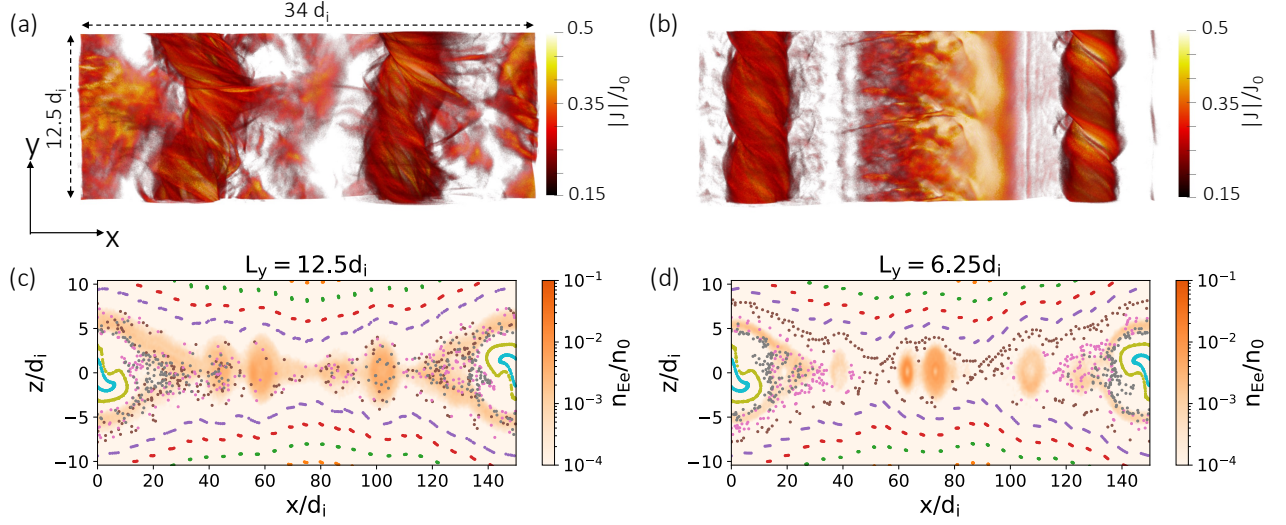


FIG. 1. Current density $|J|/en_0c$ for simulations with $L_x = 150d_i$ and different y -dimensions (a) $L_y = 12.5d_i$ and (b) $L_y = 6.25d_i$, respectively. (c) and (d) show respectively the y -averaged energetic electron density in these two simulations, overlapped with Poincaré-type plots of magnetic field lines – traced from $x = 0$ with their locations in the $x - z$ plane recorded every $6.25d_i$ in y , and with different colors for different starting points.

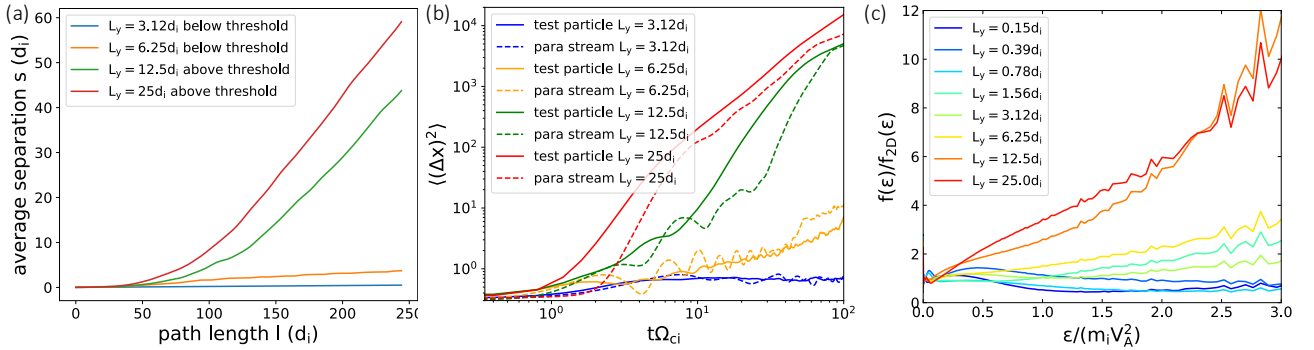


FIG. 2. (a) the averaged separation in the $x - z$ plane for 1000 pairs of initially adjacent field lines traced from the center of a flux rope with $D \sim 15d_i$. (b) the mean-square displacement in the x direction for test-particle electrons and parallel-streaming particles from the cores of flux ropes they start from. Test-particle electrons are injected with initial isotropic velocity $\sim 3.5V_A$ while the parallel-streaming particles have a parallel velocity $2V_A$ equal to the test particles' root-mean-square parallel velocity. (c) the enhancement of energetic electrons in 3D compared with a 2D simulation.

not form clear and sustainable power-laws for either species due to inefficient transport and acceleration. Therefore, $L_y > L_{th}$ also serve as a necessary condition for power-law formation. We have verified the dependence of L_{th} on guide fields using simulations with $b_g < 0.5$ and that the electron and proton spectra are insensitive to a higher proton-to-electron mass ratio 100.

Particle Acceleration Processes.— Figure 3(d) shows the energy evolution of different generations of ions and electrons. These particles are selected when their final energies are above the corresponding low-energy bound, and are grouped together and averaged as one “generation” if the starting time of particle energization is within a $\Omega_{ci}\Delta t = 5$ interval. The energy evolution of each generation suggests that accelerated particles experience an

injection process followed by a prolonged Fermi acceleration phase. The low-energy bounds of the power-laws are determined by the injection energy. When cold protons first enter the reconnection exhaust, they receive an initial kick from the outflow ($V_{out} \sim 0.5V_A$ in our simulations) and gain a speed of about $2V_{out}$ (with $\epsilon \sim \epsilon_{li}$), which boosts their energy for further acceleration. Thus at early time (e.g., $\Omega_{ci}t = 75$), most protons are bounded by ϵ_{li} in Figure 3(b), and later acceleration shapes the distribution into a power-law extending to higher energy. We have confirmed $\epsilon_{li} \sim 0.5m_i V_A^2$ with different simulations in the low- β regime ($\beta \lesssim 0.1$). On the other hand, electrons are much lighter, resulting in a less efficient energization process in the exhaust [30–33]. As a result, the electrons' low-energy bound $\epsilon_{le} \sim 4T_{ex}$, where T_{ex} is

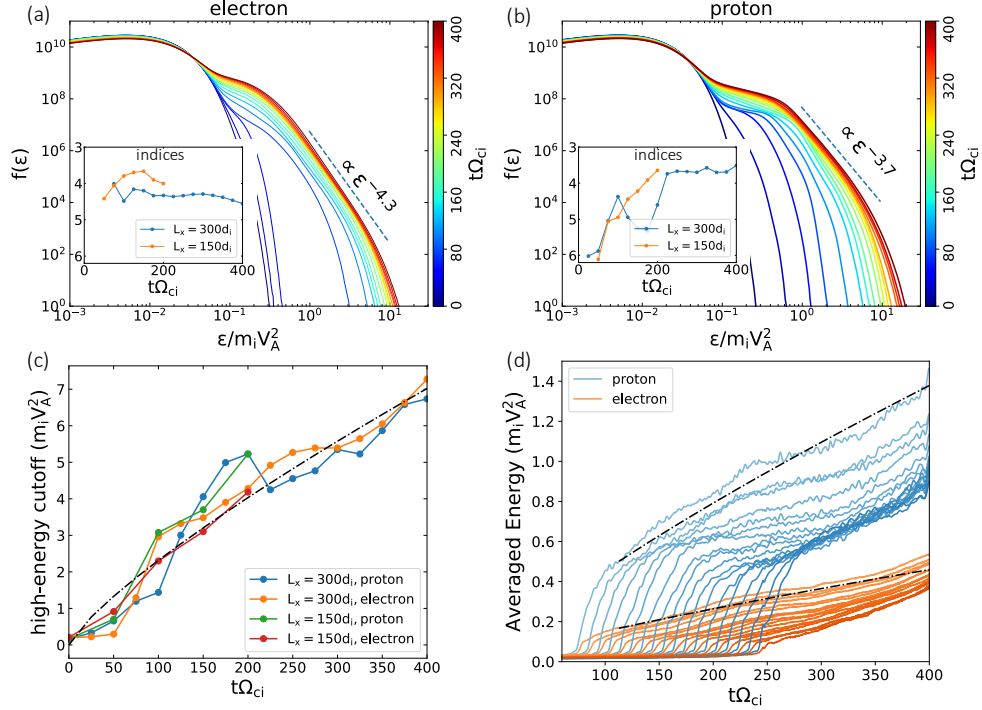


FIG. 3. Evolution of energy spectra for electrons (a) and protons (b) in the $L_x = 300d_i$ simulation. The spectral indices of this and a $L_x = 150d_i$ simulation are shown in the insets. (c) shows the high-energy cutoff of the power-laws, determined by the energy at which the spectrum deviates from the fitted power-law by 50%. (d) shows the energization history of different generations of injected particles. The dash-dot lines represent the $\varepsilon \propto t^{0.8}$ scaling in (c) and (d).

the electron temperature at the exhaust ($\sim 0.05m_i V_A^2$ in this simulation) [34].

The later Fermi acceleration process can be elucidated by the following scaling analysis. Since the Fermi acceleration rate at typical acceleration regions (exhausts) $\alpha \equiv \dot{\varepsilon}/\varepsilon \sim \mathbf{U_E} \cdot \boldsymbol{\kappa} \sim V_{Ax}\kappa_x$ and the escape rate from the reconnection layer $\tau_{esc}^{-1} \sim V_{Ax}/L$, the power-law index [35, 36]

$$p = 1 + (\alpha\tau_{esc})^{-1} \sim 1 + \frac{V_{Ax}/L}{V_{Ax}\kappa_x} = 1 + \frac{1}{L\kappa_x}, \quad (1)$$

where $\mathbf{U_E}$ is the $\mathbf{E} \times \mathbf{B}$ drift speed, $\boldsymbol{\kappa}$ is the magnetic field curvature vector and L is the half length of the reconnecting current sheet. Using $\kappa_x = (\hat{b} \cdot \nabla \hat{b})_x \sim \hat{b}_z \cdot \partial_z \hat{b}_x \sim B_z B_x / B^2 / \Delta_z$, where Δ_z is the typical length scale in z of exhaust field lines (related to the scale of flux ropes), we obtain

$$p \sim 1 + \frac{B_x}{B_z} \frac{\Delta_z}{L} \left(1 + \frac{B_g^2}{B_x^2}\right). \quad (2)$$

$$\alpha \sim V_{Ax}\kappa_x = \frac{B_z V_{Ax} B_x^2}{B_x (B_x^2 + B_g^2) \Delta_z}. \quad (3)$$

Since both Δ_z and L are proportional to the reconnection domain, in larger simulations the predicted spectral

indices remain the same. In the acceleration regions (exhausts), taking $B_g^2/B_x^2 \ll 1$, $B_z \sim 0.05B_x$, $\Delta_z/L \sim 0.15$ typical during our simulations, we obtain $p \sim 4$, which is comparable to particle spectral indices in our simulations. Since flux ropes grow over time, Δ_z increases (nearly linearly) and leads to a decrease in the acceleration rate $\alpha \sim C/t$, where C is a constant. More careful inspection to the time evolution of Δ_z in simulations suggests $C \sim 0.8$ (not shown). We also measure the acceleration rates directly from simulations as in Li et al. [13], finding values and dependence on time and simulation size roughly consistent with the theoretical prediction. From the acceleration rate above, we obtain particle energy $\varepsilon \propto t^{0.8}$. This scaling agrees reasonably well with the growth of high-energy cutoffs (Figure 3(c)) and particle energy evolution (Figure 3(d)) in the simulation. These demonstrate that electrons and protons are both accelerated by Fermi acceleration into power-law particle spectra, consistent with the highly correlated ion acceleration and electron acceleration observed in solar flares [5].

Discussion.— While observations have suggested efficient acceleration of both electrons and ions during non-relativistic reconnection in solar flares and the magnetotail, establishing this from first principles kinetic simulations has been a long-standing challenge. For the first time, our simulations produce power-law distributions

for both electrons and protons that contain a significant amount of released magnetic energy, providing a plausible explanation to the solar flare observations [2–4, 27–29]. The $p \sim 4$ spectra obtained in our simulations are consistent with the electron indices inferred from a large number of x-ray and microwave observations [4, 37], and the proton indices from gamma-ray [3] and SEP observations [38]. For the September 10, 2017 event observed by numerous instruments, comparison between MHD simulations and gyrosynchrotron emission suggests magnetic reconnection occurred with a weak guide field ($b_g \sim 0.3$) [39]. Evidence of turbulent reconnection has been presented [40, 41] for this event and the spectral index obtained by gyrosynchrotron emission in the current sheet is $p \sim 3.5 - 6.5$, broadly consistent with our simulations. Our simulations can also be compared positively with a well observed magnetotail event recently reported by Magnetospheric Multi-scale Mission (MMS) [6, 7]. The event shows simultaneous electron and proton nonthermal acceleration in a broad turbulent reconnection region over ~ 16 Earth radii ($\sim 80d_i$) with a low upstream β ($\beta_e \sim 0.03$), which is quite similar to our simulations. The observed power-law indices are typically $\sim 3.3 - 4.3$ for protons and $\sim 4.2 - 5.4$ for electrons, in agreement with our simulations. The shoulders of the observed spectra are ~ 15 keV ($0.2m_i V_A^2$) for electrons and ~ 40 keV ($0.6m_i V_A^2$) for protons, also similar to our simulations. In addition, protons are observed to gain more energy than electrons.

We have demonstrated that flux-rope kink instability drives strong field-line chaos in 3D reconnection with weak guide fields, leading to strong particle transport and acceleration. As a result, both electrons and protons are accelerated into clear power-law spectra, whose basic properties such as efficiency and spectral indices are controlled by the injection and Fermi acceleration processes. The formation of the power-laws, especially protons, requires large domain size in the reconnection plane and long acceleration time, as well as sufficient 3D physics to

capture the flux rope $m = 1$ kink instability. This work uncovers the fundamental processes for initializing and developing nonthermal ion and electron acceleration in nonrelativistic magnetic reconnection, with strong implications not only to heliophysics but also other astrophysical phenomena such as stellar flares.

Acknowledgment.— We gratefully acknowledge the helpful discussions in the SolFER DRIVE Science Center collaboration. Q.Z, F.G., W.D. and H.L. acknowledge the support from Los Alamos National Laboratory through the LDRD program and its Center for Space and Earth Science (CSES), and NASA programs through grant NNH17AE68I, 80HQTR20T0073, 80NSSC20K0627, and 80HQTR21T0005, and through Astrophysical Theory Program. The work by X.L. is funded by the National Science Foundation grant PHY-1902867 through the NSF/DOE Partnership in Basic Plasma Science and Engineering and NASA MMS 80NSSC18K0289. The simulations used resources provided by the Los Alamos National Laboratory Institutional Computing Program, the National Energy Research Scientific Computing Center (NERSC) and the Texas Advanced Computing Center (TACC).

SUPPLEMENTAL MATERIAL

Table S1 lists information of all simulations discussed in this paper with a broad range of parameters. Using a large set of fully kinetic simulations (Runs 1-15), we verified the threshold $L_{th} \sim \pi b_g D \sim 0.1\pi b_g L_x$ for the development of flux-rope kink instability and the field-line chaos, which is a necessary condition for the power-law formation. Runs 1-11 are used to verify the dependence on domain size, while additional Runs 12-15 are for verifying the dependence on guide fields in the weak-guide-field regime. With Run 16, we also confirmed the low-energy bounds of proton power-laws $\varepsilon_{li} \sim 0.5m_i V_A^2$ as long as $\beta \lesssim 0.1$. With Runs 17-18, we also verified that the electron and proton spectra are insensitive to mass ratios.

* qlzhanggo@gmail.com

- [1] M. Yamada, R. Kulsrud, and H. Ji, Magnetic Reconnection, *Rev. Mod. Phys.* **82**, 603 (2010).
- [2] R. P. Lin, Energy Release and Particle Acceleration in Flares: Summary and Future Prospects, *Space Sci. Rev.* **159**, 421 (2011).
- [3] N. Omodei, M. Pesce-Rollins, F. Longo, A. Allafort, and S. Krucker, Fermi -LAT Observations of the 2017

September 10 Solar Flare, *ApJ* **865**, L7 (2018).

- [4] D. E. Gary, B. Chen, B. R. Dennis, G. D. Fleishman, G. J. Hurford, S. Krucker, J. M. McTiernan, G. M. Nita, A. Y. Shih, S. M. White, and S. Yu, Microwave and Hard X-Ray Observations of the 2017 September 10 Solar Limb Flare, *ApJ* **863**, 83 (2018).
- [5] A. Y. Shih, R. P. Lin, and D. M. Smith, RHESSI Observations of the Proportional Acceleration of Relativistic >0.3 MeV Electrons and >30 MeV Protons in Solar Flares, *ApJ* **698**, L152 (2009).

Run	L_x/d_i	L_y/d_i	L_z/d_i	β_e	B_g/B_0	m_i/m_e	L_{th}/d_i	m=1 kink unstable
1	300	25.0	125.0	0.02	0.2	25	19	Yes
2	300	12.5	125.0	0.02	0.2	25	19	No
3	150	25.0	62.5	0.02	0.2	25	9.5	Yes
4	150	12.5	62.5	0.02	0.2	25	9.5	Yes
5	150	6.25	62.5	0.02	0.2	25	9.5	No
6	150	3.125	62.5	0.02	0.2	25	9.5	No
7	150	1.5625	62.5	0.02	0.2	25	9.5	No
8	150	0.7813	62.5	0.02	0.2	25	9.5	No
9	150	0.3906	62.5	0.02	0.2	25	9.5	No
10	150	0.1465	62.5	0.02	0.2	25	9.5	No
11	150	0.0488	62.5	0.02	0.2	25	9.5	No
12	150	18.75	62.5	0.02	0.3	25	14.25	Yes
13	150	9.375	62.5	0.02	0.3	25	14.25	No
14	150	7.8125	62.5	0.02	0.1	25	4.75	Yes
15	150	3.125	62.5	0.02	0.1	25	4.75	No
16	150	12.5	62.5	0.08	0.2	25	9.5	Yes
17	75	6.25	31.25	0.02	0.2	25	4.75	Yes
18	75	6.25	31.25	0.02	0.2	100	4.75	Yes

TABLE S1. All simulations discussed in this paper.

- [6] R. E. Ergun, K. A. Goodrich, F. D. Wilder, N. Ahmadi, J. C. Holmes, S. Eriksson, J. E. Stawarz, R. Nakamura, K. J. Genestreti, M. Hesse, J. L. Burch, R. B. Torbert, T. D. Phan, S. J. Schwartz, J. P. Eastwood, R. J. Strangeway, O. Le Contel, C. T. Russell, M. R. Argall, P. A. Lindqvist, L. J. Chen, P. A. Cassak, B. L. Giles, J. C. Dorelli, D. Gershman, T. W. Leonard, B. Lavraud, A. Retino, W. Matthaeus, and A. Vaivads, Magnetic Reconnection, Turbulence, and Particle Acceleration: Observations in the Earth's Magnetotail, *Geophys. Res. Lett.* **45**, 3338 (2018).
- [7] R. E. Ergun, N. Ahmadi, L. Kromyda, S. J. Schwartz, A. Chasapis, S. Hoilijoki, F. D. Wilder, J. E. Stawarz, K. A. Goodrich, D. L. Turner, I. J. Cohen, S. T. Bingham, J. C. Holmes, R. Nakamura, F. Pucci, R. B. Torbert, J. L. Burch, P. A. Lindqvist, R. J. Strangeway, O. Le Contel, and B. L. Giles, Observations of Particle Acceleration in Magnetic Reconnection-driven Turbulence, *ApJ* **898**, 154 (2020).
- [8] J. F. Drake, M. Swisdak, H. Che, and M. A. Shay, Electron Acceleration from Contracting Magnetic Islands during Reconnection, *Nature* **443**, 553 (2006).
- [9] J. T. Dahlin, J. F. Drake, and M. Swisdak, The Mechanisms of Electron Heating and Acceleration during Magnetic Reconnection, *Phys. Plasmas* **21**, 092304 (2014).
- [10] J. T. Dahlin, J. F. Drake, and M. Swisdak, The Role of Three-dimensional Transport in Driving Enhanced Electron Acceleration during Magnetic Reconnection, *Phys. Plasmas* **24**, 92110 (2017).
- [11] X. Li, F. Guo, H. Li, and G. Li, Particle Acceleration during Magnetic Reconnection in a Low-beta Plasma, *ApJ* **843**, 21 (2017).
- [12] X. Li, F. Guo, H. Li, and J. Birn, The Roles of Fluid Compression and Shear in Electron Energization during Magnetic Reconnection, *ApJ* **855**, 80 (2018), arXiv:1801.02255 [physics.plasm-ph].
- [13] X. Li, F. Guo, H. Li, A. Stanier, and P. Kilian, Formation of Power-law Electron Energy Spectra in Three-dimensional Low- β Magnetic Reconnection, *ApJ* **884**, 118 (2019), arXiv:1909.01911 [astro-ph.SR].
- [14] H. Arnold, J. F. Drake, M. Swisdak, F. Guo, J. T. Dahlin, B. Chen, G. Fleishman, L. Glesener, E. Kontar, T. Phan, and C. Shen, Electron Acceleration during Macroscale Magnetic Reconnection, *Phys. Rev. Lett.* **126**, 135101 (2021), arXiv:2011.01147 [physics.plasm-ph].
- [15] K. Bowers and H. Li, Spectral Energy Transfer and Dissipation of Magnetic Energy from Fluid to Kinetic Scales, *Phys. Rev. Lett.* **98**, 035002 (2007).
- [16] W. Daughton, V. Roytershteyn, H. Karimabadi, L. Yin, B. J. Albright, B. Bergen, and K. J. Bowers, Role of Electron Physics in the Development of Turbulent Magnetic Reconnection in Collisionless Plasmas, *Nature Physics* **7**, 539 (2011).
- [17] Y.-H. Liu, W. Daughton, H. Karimabadi, H. Li, and V. Roytershteyn, Bifurcated Structure of the Electron Diffusion Region in Three-Dimensional Magnetic Reconnection, *Phys. Rev. Lett.* **110**, 265004 (2013).
- [18] M. Onofri, H. Isliker, and L. Vlahos, Stochastic Acceleration in Turbulent Electric Fields Generated by 3D Reconnection, *Phys. Rev. Lett.* **96**, 151102 (2006), arXiv:astro-ph/0604192 [astro-ph].
- [19] J. T. Dahlin, J. F. Drake, and M. Swisdak, Electron Acceleration in Three-dimensional Magnetic Reconnection with a Guide Field, *Phys. Plasmas* **22**, 100704 (2015).
- [20] K. J. Bowers, B. J. Albright, L. Yin, B. Bergen, and T. J. T. Kwan, Ultrahigh Performance Three-dimensional Electromagnetic Relativistic Kinetic Plasma Simulation, *Phys. Plasmas* **15**, 055703 (2008).
- [21] The rendering has used a lower limit of $|J|$ to filter the upstream contents and emphasize the central regions of flux ropes to better visualize their motions.
- [22] Note that the domain in Figure 1(b) has been replicated in the y direction as it is periodic to better compare with Figure 1(a).
- [23] E. Oz, C. E. Myers, M. Yamada, H. Ji, R. M. Kulsrud, and J. Xie, Experimental Verification of The Kruskal-Shafranov Stability Limit in Line-tied Partial-toroidal Plasmas, *Phys. Plasmas* **18**, 102107 (2011).
- [24] In contrast to the overlapping oblique tearing modes in the strong guide field regime [16].

- [25] L. Yang, H. Li, F. Guo, X. Li, S. Li, J. He, L. Zhang, and X. Feng, Fast Magnetic Reconnection with Turbulence in High Lundquist Number Limit, *ApJL* **901**, L22 (2020).
- [26] F. Guo, X. Li, W. Daughton, H. Li, P. Kilian, Y.-H. Liu, Q. Zhang, and H. Zhang, Magnetic Energy Release, Plasma Dynamics and Particle Acceleration during Relativistic Turbulent Magnetic Reconnection, *arXiv e-prints*, arXiv:2008.02743 (2020), arXiv:2008.02743 [astro-ph.HE].
- [27] S. Krucker, H. S. Hudson, L. Glesener, S. M. White, S. Masuda, J. P. Wuelser, and R. P. Lin, Measurements of the Coronal Acceleration Region of a Solar Flare, *ApJ* **714**, 1108 (2010).
- [28] M. Oka, S. Krucker, H. S. Hudson, and P. Saint-Hilaire, Electron Energy Partition in the Above-the-loop-top Solar Hard X-Ray Sources, *ApJ* **799**, 129 (2015).
- [29] M. J. Aschwanden, G. Holman, A. O’Flannagain, A. Caspi, J. M. McTiernan, and E. P. Kontar, Global Energetics of Solar Flares. III. Nonthermal Energies, *ApJ* **832**, 27 (2016), arXiv:1607.06488 [astro-ph.SR].
- [30] T. D. Phan, M. A. Shay, J. T. Gosling, M. Fujimoto, J. F. Drake, G. Paschmann, M. Øieroset, J. P. Eastwood, and V. Angelopoulos, Electron Bulk Heating in Magnetic Reconnection at Earth’s Magnetopause: Dependence on the Inflow Alfvén Speed and Magnetic Shear, *Geophys. Res. Lett.* **40**, 4475 (2013).
- [31] M. A. Shay, C. C. Haggerty, T. D. Phan, J. F. Drake, P. A. Cassak, P. Wu, M. Øieroset, M. Swisdak, and K. Malakit, Electron Heating during Magnetic Reconnection: A Simulation Scaling Study, *Phys. Plasmas* **21**, 122902 (2014).
- [32] Q. Zhang, J. F. Drake, and M. Swisdak, Particle Heating and Energy Partition in Low- β Guide Field Reconnection with Kinetic Riemann Simulations, *Phys. Plasmas* **26**, 072115 (2019), arXiv:1904.12922 [physics.plasm-ph].
- [33] Q. Zhang, J. F. Drake, and M. Swisdak, Instabilities and Turbulence in Low- β Guide Field Reconnection Exhausts with Kinetic Riemann Simulations, *Phys. Plasmas* **26**, 102115 (2019), arXiv:1907.03181 [physics.plasm-ph].
- [34] In principle, T_{ex} can depend on a broad range of parameters (β , $m_i V_A^2$, B_g , etc.), which is out of the scope of this Letter and will be further studied in the future.
- [35] L. O. Drury, P. Duffy, D. Eichler, and A. Mastichiadis, On “Box” Models of Shock Acceleration and Electron Synchrotron Spectra, *A&A* **347**, 370 (1999), arXiv:astro-ph/9905178 [astro-ph].
- [36] F. Guo, H. Li, W. Daughton, and Y.-H. Liu, Formation of Hard Power Laws in the Energetic Particle Spectra Resulting from Relativistic Magnetic Reconnection, *Phys. Rev. Lett.* **113**, 155005 (2014).
- [37] M. Oka, J. Birn, M. Battaglia, C. C. Chaston, S. M. Hatch, G. Livadiotis, S. Imada, Y. Miyoshi, M. Kuhar, F. Effenberger, E. Eriksson, Y. V. Khotyaintsev, and A. Retinò, Electron Power-Law Spectra in Solar and Space Plasmas, *Space Sci. Rev.* **214**, 82 (2018), arXiv:1805.09278 [astro-ph.SR].
- [38] C. M. S. Cohen *et al.*, Parker Solar Probe Observations of He/H Abundance Variations in SEP Events inside 0.5 AU, *A&A* 10.1051/0004-6361/202039299 (2020).
- [39] B. Chen, C. Shen, D. E. Gary, K. K. Reeves, G. D. Fleishman, S. Yu, F. Guo, S. Krucker, J. Lin, G. M. Nita, and X. Kong, Measurement of Magnetic Field and Relativistic Electrons along a Solar Flare Current Sheet, *Nature Astronomy* **4**, 1140 (2020), arXiv:2005.12757 [astro-ph.SR].
- [40] X. Cheng, Y. Li, L. F. Wan, M. D. Ding, P. F. Chen, J. Zhang, and J. J. Liu, Observations of Turbulent Magnetic Reconnection within a Solar Current Sheet, *ApJ* **866**, 64 (2018), arXiv:1808.06071 [astro-ph.SR].
- [41] R. J. French, P. G. Judge, S. A. Matthews, and L. van Driel-Gesztelyi, Spectropolarimetric Insight into Plasma Sheet Dynamics of a Solar Flare, *ApJL* **887**, L34 (2019), arXiv:1911.12666 [astro-ph.SR].